Akeret *et al. Journal of Neuroinflammation* (2022) 19:290
https://doi.org/10.1186/s12974-022-02641-5

Journal of Neuroinflammation

RESEARCH

Open Access

# MyD88-TLR4-dependent choroid plexus activation precedes perilesional inflammation and secondary brain edema in a mouse model of intracerebral hemorrhage

Kevin Akeret[1†], Raphael M. Buzzi[2†], Bart R. Thomson[1,2], Nina Schwendinger[1,2], Jan Klohs[3], Nadja Schulthess-Lutz[2], Livio Baselgia[2], Kerstin Hansen[2], Luca Regli[1], Florence Vallelian[2], Michael Hugelshofer[1*†] and Dominik J. Schaer[2†]

## Abstract

**Background:** The functional neurological outcome of patients with intracerebral hemorrhage (ICH) strongly relates to the degree of secondary brain injury (ICH-SBI) evolving within days after the initial bleeding. Different mechanisms including the incitement of inflammatory pathways, dysfunction of the blood–brain barrier (BBB), activation of resident microglia, and an influx of blood-borne immune cells, have been hypothesized to contribute to ICH-SBI. Yet, the spatiotemporal interplay of specific inflammatory processes within different brain compartments has not been sufficiently characterized, limiting potential therapeutic interventions to prevent and treat ICH-SBI.

**Methods:** We used a whole-blood injection model in mice, to systematically characterized the spatial and temporal dynamics of inflammatory processes after ICH using 7-Tesla magnetic resonance imaging (MRI), spatial RNA sequencing (spRNAseq), functional BBB assessment, and immunofluorescence average-intensity-mapping.

**Results:** We identified a pronounced early response of the choroid plexus (CP) peaking at 12–24 h that was characterized by inflammatory cytokine expression, epithelial and endothelial expression of leukocyte adhesion molecules, and the accumulation of leukocytes. In contrast, we observed a delayed secondary reaction pattern at the injection site (striatum) peaking at 96 h, defined by gene expression corresponding to perilesional leukocyte infiltration and correlating to the delayed signal alteration seen on MRI. Pathway analysis revealed a dependence of the early inflammatory reaction in the CP on toll-like receptor 4 (TLR4) signaling via myeloid differentiation factor 88 (MyD88). TLR4 and MyD88 knockout mice corroborated this observation, lacking the early upregulation of adhesion molecules and leukocyte infiltration within the CP 24 h after whole-blood injection.

†Kevin Akeret and Raphael M. Buzzi contributed equally to this work.

†Michael Hugelshofer and Dominik J. Schaer share last authorship.

*Correspondence: michael.hugelshofer@usz.ch

[1] Department of Neurosurgery, Clinical Neuroscience Center, Universitätsspital and University of Zurich, Frauenklinikstrasse 10, 8091 Zurich, Switzerland
Full list of author information is available at the end of the article

**Conclusions:** We report a biphasic brain reaction pattern after ICH with a MyD88-TLR4-dependent early inflammatory response of the CP, preceding inflammation, edema and leukocyte infiltration at the lesion site. Pharmacological targeting of the early CP activation might harbor the potential to modulate the development of ICH-SBI.

**Keywords:** Neuroinflammation, Secondary brain injury, Glymphatics, Spatial RNA sequencing, Quantitative histology

## Introduction

Intracerebral hemorrhage (ICH) accounts for 15–20% of all strokes [1]. ICH is less common than ischemic stroke but results in substantially higher morbidity and mortality [2]. While the acute mass effect of a hemorrhage leads to immediate mechanical brain damage, functional neurological outcomes are strongly related to the occurrence of secondary brain injury (ICH-SBI) that evolves within days or a few weeks after the initial ICH [3]. Perihemorrhagic edema is a radiological surrogate for ICH-SBI that correlates with the need for surgical rescue measures and a poor clinical outcome [4]. Mechanisms that have been hypothesized to contribute to perihemorrhagic edema and ICH-SBI include the incitement of inflammatory pathways, dysfunction of the blood–brain barrier (BBB), activation of resident microglia, and an influx of blood-borne immune cells [5]. However, the spatial and temporal interplay of specific inflammatory processes after ICH has not been sufficiently characterized, limiting targeted interventions to prevent and treat ICH-SBI [6].

There are three compartments of decreasing immune privilege in the brain: brain parenchyma, cerebrospinal fluid (CSF) space, and leptomeninges, including the choroid plexus (CP) as an intraventricular evagination [7]. While the CP was long considered as an exclusively secretory organ for CSF, there is growing evidence for an immunological role in the pathogenesis of various neurological conditions [8, 9]. The CP is a highly vascularized convolute located in the ventricular system composed of a monolayered epithelium and a stromal core [10]. Microvilli on the CSF side of the CP epithelium create an enormous apical surface area, which corresponds to approximately 10% of the BBB [10, 11]. The perfusion of the CP stroma is the highest within the entire brain [12]. Given its central location in the brain, its enormous contact area with both the CSF and peripheral circulation, and its extensive perfusion, we hypothesize that the CP plays a pivotal role in the regulation of inflammatory processes after ICH.

Using a whole-blood striatal injection mouse model, this study explored the spatial and temporal dynamics of inflammatory processes after ICH using 7-Tesla magnetic resonance imaging (MRI), spatial RNA sequencing (spRNAseq), functional BBB assessment, and immunofluorescence average-intensity mapping. Our data revealed a biphasic brain reaction pattern, including a distinct early inflammatory response of the CP, which preceded inflammation and leukocyte infiltration at the lesion site. The post-hemorrhagic CP response was dependent on toll-like receptor 4 (TLR4) signaling via myeloid differentiation factor 88 (MyD88).

## Methods

### Experiment series and animals

The experiments were organized into temporal and MyD88-TLR4 series. Temporal series investigated the spatiotemporal dynamics after striatal whole-blood injection using MRI, spRNAseq, and immunohistology. All temporal experiments were performed using 10- to 12-week-old wild-type C57BL/6J mice ($n_{MRI}=10$, $n_{spRNAseq}=6$, $n_{Immunohistology}=21$). The inflammatory CP response findings determined the time point and specific readouts used in the MyD88-TLR4 series. For the latter, we used 10- to 12-week-old MyD88 ($n=8$, B6.129P2-Tlr4<tm1Aki>) and TLR4 ($n=6$, B6-MyD88<tm1Aki>) knockout mice with wild-type littermate controls ($n_{MyD88+/+}=16$, $n_{TLR4+/+}=12$). All experiments were approved by the Swiss Federal Veterinary Office (ZH89/2019). Mice were obtained from Charles River Laboratories (Sulzfeld, Germany) and housed in individually ventilated cages within the Laboratory Animal Services Center at the University of Zurich with a 12-h/12-h dark/light cycle.

### Randomization and blinding

Group allocation (time points, injection fluid) was based on simple randomization using R (version 4.0.3) [13]. Investigators were blinded to group allocation.

### Striatal injection model

Whole blood was collected from deeply anesthetized mice by terminal cardiac puncture, anticoagulated with sodium citrate and used immediately. Stereotactic striatal needle insertion followed a previously published protocol [14, 15]. We inserted a 33-G needle with a speed of 0.1 mm/s. 10 µL of fluid was injected with 2000 nL/min. The needle was left in place for 10 min, then removed slowly (0.1 mm/s) and the skin sutured. After surgery, the animals were placed in a heated wake-up box and monitored until they were fully recovered and could be transferred back to their cage.

### Magnetic resonance imaging

MRI data were collected at different time points (2, 24, 48, 96 h) after surgery in the same mice, using a 7/16 small animal MR scanner (Pharmascan, Bruker Biospin GmbH, Ettlingen, Germany). Detailed technical and procedural information are provided in the Additional file 1.

### Cryosections

For spRNAseq analysis, mice were transcardially perfused with 50 mL of ice-cold phosphate buffered saline (PBS) at different time points (2, 12, 24, 48, 96 h) after striatal whole-blood injection. The brain was extracted and immediately flash-frozen in cold Tissue-Tek OCT Compound (Sakura Finetek, Netherlands) using a liquid nitrogen-cooled metal block and stored at − 80 °C until sectioning. We maintained the time from brain extraction to freezing below 1 min. Using a Leica CM3050 S Cryostat (Leica, Germany), 10-µm coronal cryosections were prepared and placed within the etched frames of the capture areas on the active surface of the Visium Spatial Slide (10X Genomics, Pleasanton, CA, USA).

### Spatial RNA sequencing

Tissue processing was performed according to the manufacturer's instructions (User Guide CG000239, Rev A) [14]. Sections were fixed with cold methanol (− 20 °C) and stained with H&E. Prior to permeabilization, we obtained brightfield images of the stained sections using an Axio Observer (Zeiss, Germany). Then, tissue sections were permeabilized for 6 min, followed by reverse transcription, second-strand synthesis, denaturation, complementary DNA (cDNA) amplification, and SPRIselect (Beckman Coulter, Brea, CA, USA) cDNA cleanup. Finally, cDNA libraries were prepared and sequenced on an Illumina NovaSeq 6000 (Illumina, San Diego, CA, USA) using a 28 + 120 bp paired-end sequencing mode.

Mapping and counting were performed using Space Ranger 1.1.0 (10X Genomics), with the reference genome GRCm38.p6 (mm10). Space Ranger aligned the barcodes in each read with a feature (i.e., a single spot with 55 µm diameter on the slide with a distinct spatial position defined by a unique barcode) relative to the fiducial frame, thereby associating read counts with spatial location and histological image. Downstream analysis was performed in python using the workflow and packages described in the Additional file 1 [16].

### Immunohistology

Immunohistological analyses were coupled to an assessment of the BBB. Mice received an intraperitoneal injection of a fluorescently labeled dextran diluted in 0.9% saline solution (Additional file 1: Table S1) 2 h before euthanasia. For euthanasia, mice were deeply anesthetized with intraperitoneal injection of ketamine/xylazine/acepromazine and transcardially perfused with 0.1 M PBS followed by 30 mL ice-cold 4% paraformaldehyde in PBS. After removal of the brain and post-fixation overnight in 4% paraformaldehyde at 4 °C, brains were cut into 60-µm histological sections using a vibratome (VT1000 S; Leica, Geneva, Switzerland). For quantification, a standardized selection of eight sections across the lesion (every second section, beginning at 300 µm posterior to the anterior commissure) was collected. Incubation with primary antibodies was performed over 48 h at 4 °C, followed by secondary antibodies over 24 h at 4 °C and Hoechst staining for 40 min. Between each staining step, slices were washed three times. After mounting with ProLong Gold (Invitrogen, CA, USA), imaging was performed using the Axio Scan.Z1 (Zeiss, Oberkochen, Germany). The antibodies and the dilutions used for staining are listed in Additional file 1: Table S2.

### Histological quantification

To achieve a reproducible representation of the lesion, the CP, and the cerebral hemisphere, histological quantification was performed on a selection of eight anatomically standardized coronal sections per mouse (every second section, beginning at 300 µm posterior to the anterior commissure). Leakage area size and intensity were semi-automatically quantified by two blinded investigators with a custom-made Fiji plugin [15]. Average-intensity-maps were calculated in a python environment after manual segmentation of the different anatomical compartments by two blinded investigators as described in the Additional file 1.

### Data visualization and statistical analysis

Statistical analysis was performed using R (version 4.0.2) [13]. In the temporal series, for each time point a 95% bootstrap confidence interval was calculated and visualized as a box. As a summary, a loess curve was fitted to the data using a t-based approximation and plotted as a line. In the knockout series, the boxplots represent group averages on an animal level. The box bounds the interquartile range (IQR) divided by the median, while the whiskers extend to the highest and lowest value within the 1.5 IQR, respectively.

### Data and code availability

The Fiji-script, processed spRNAseq-data, python script, and R-code to reproduce all analyses and plots are available online (https://doi.org/10.5281/zenodo.5760872).

## Results

### Striatal whole-blood injection evokes a biphasic injury phenotype

First, MR-morphological and hematoxylin and eosin (H&E) histological changes were investigated 2, 24, 48, and 96 h after striatal whole-blood injection (Fig. 1A). Serial T2-weighted and susceptibility-weighted images (SWI) demonstrated an acute transient T2/SWI signal change at 24 h (Fig. 1B). A secondary phase of T2/SWI-hypointensity was consistently detected at 96 h. The H&E appearance of the lesion remained largely unchanged up to 48 h post-injection with only sparse cellular infiltration (Fig. 1C). From 48 to 96 h, there was a substantial reduction of the blood clot area associated with increased cellularity at the lesion site. Intraventricular hemorrhage was found in 3/10 animals (30%) based on the initial SWI. Collectively, MRI demonstrated a biphasic injury phenotype with a secondary signal alteration coinciding with histological evidence of cellular infiltration and hematoma resolution.

### Transcriptional changes to striatal whole-blood injection

Next, we explored spatial transcriptome changes after striatal whole-blood injection applying the 10 × Genomics workflow while focusing on the brain regions comprising the perilesional area (striatum) and the CP. This approach allowed the extraction of gene expression data from these specific brain regions, which are otherwise difficult to selectively isolate. We obtained spRNAseq data from a control mouse (no injection) and from mice 2, 12, 48, and 96 h after whole-blood injection. Per-spot gene expression data from all animals were merged into a combined dataset comprising 22′835 features. Each feature represented the gene expression pattern of the underlying tissue with a diameter of 55 µm. Aiming at an unbiased spatial segmentation of the striatum and CP, we used unsupervised clustering and predefined gene sets [17] to assign each feature to an anatomical region. Figure 2A illustrates a Uniform Manifold Approximation and Projection (UMAP) with a Leiden clustering restricted to five main clusters. We calculated gene scores for eight different anatomical regions (Fig. 2B). Four of the five clusters (1–4) matched to a single region (Fig. 2C). Cluster 0 (blue) had an association with four regions (pallidum, hypothalamus, midbrain, pons), collectively defined as deep brain structures. The correct anatomical annotation of the gene expression features was confirmed by back-projection and anatomical data visualization (Fig. 2D, Additional file 1: Fig. S2A).

Objective anatomical segmentation enabled a regionally stratified analysis of temporal gene expression changes. Within the five regions, we performed a differential gene expression analysis comparing each post-injection time point with the untouched control mouse (Fig. 2E, F, Additional file 1: Fig. S2B). Heatmaps in Fig. 2E, F illustrate the expression of the top five differentially expressed genes per time point and region. The CP and the striatum shared a very similar early transcriptional signal, with gene expressions of red blood cell components (hemoglobin, Alas2) peaking at 2 h post-injection, followed by a number of inflammatory gene expressions spiking at 12 h. This indicated that both regions were directly exposed to the injected blood or its degradation products and that these exposures evoked an acute transcriptional reaction. The red blood cell signal disappeared within 24 h, coinciding with the disappearance of the immediate post-injection signal alteration in MRI. In contrast to this early phase, the CP and the striatum differed in their gene expression patterns at later time points. The CP demonstrated a monophasic activation: after a clearly defined first gene expression wave spiking at 12–24 h, only few genes were reaching an expression peak at 48 or 96 h. In contrast, the striatum demonstrated a biphasic response, with a defined secondary wave of gene expression peaking at 96 h. This delayed response correlated with the second signal alteration on MRI at 96 h and is consistent with a delayed inflammatory reaction at the injection site.

### Early inflammatory signaling in the CP following striatal whole-blood injection

Using hallmark genes, we investigated the principal biological processes contributing to the transcriptional responses in the CP and the perilesional site. The marker genes, identified by the differential gene expression analysis, could be assigned to six different biological processes (Fig. 3A). The initial cytokine upregulation (e.g., Cxcl10, Ccl5), with a peak at 12 h, was similar in both compartments. However, compared to the perilesional area, the CP featured a more pronounced early increase of interferon response elements (e.g., Irf7, Ifi27l2a) (Fig. 3B) and cell adhesion molecules (e.g., Vcam1, Bst2) (Fig. 3C) peaking between 12 and 24 h. This was accompanied by a peak in the inflammatory response genes (Serpina3n, Lcn2). The perilesional site, in contrast, displayed a delayed increase in the same inflammatory markers peaking at 96 h (Fig. 3A). This delayed response of the perilesional site was accompanied by an increased expression of macrophage markers (Cd68, Lyz2) (Fig. 3D) and genes involved in heme/iron metabolism (Hmox1, Ftl1). The early inflammatory reaction with cytokine signaling, adhesion molecule expression, and leukocyte attraction in the CP was confirmed by selected marker genes. Both Ccl20, a chemokine expressed by

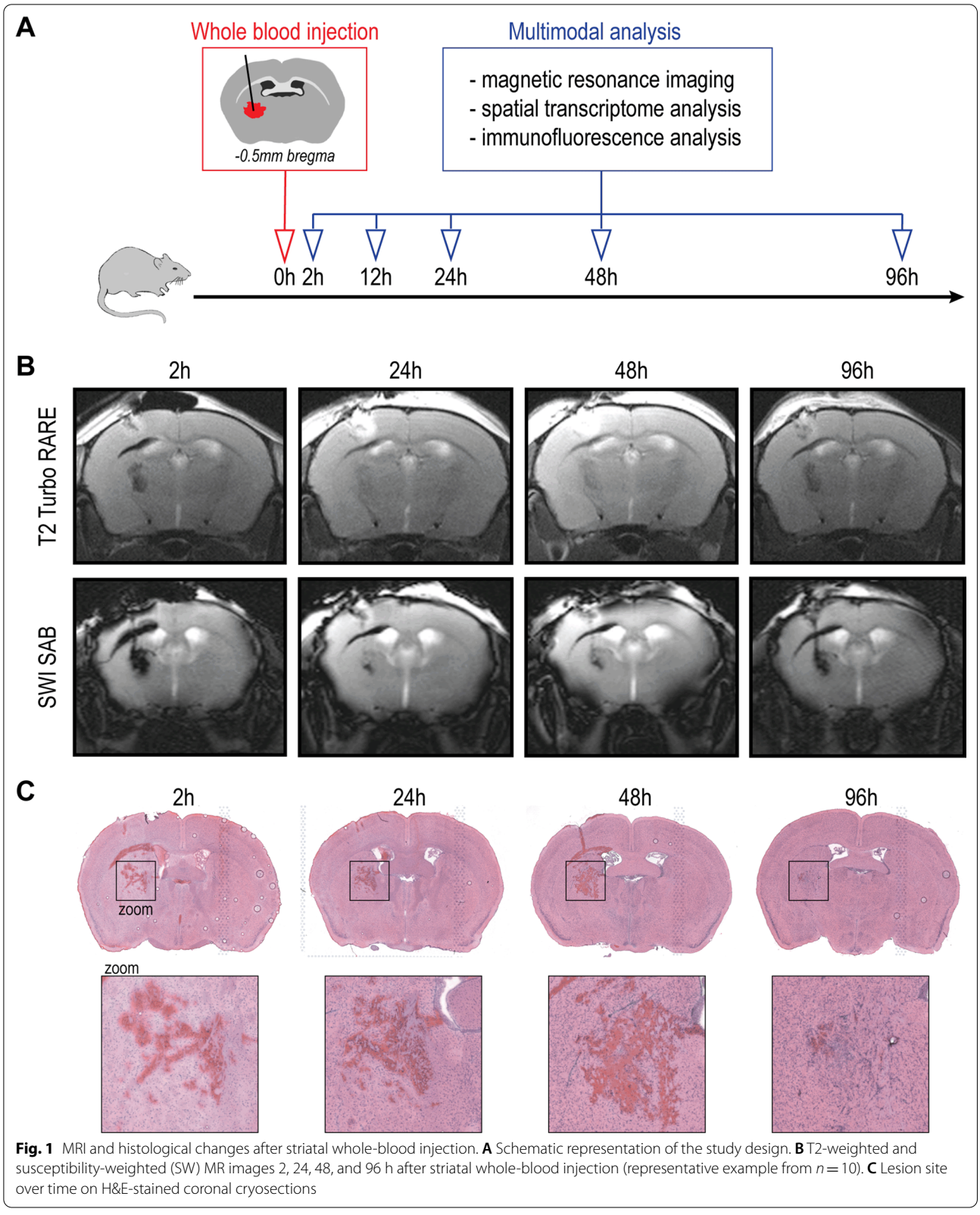


**Fig. 1** MRI and histological changes after striatal whole-blood injection. **A** Schematic representation of the study design. **B** T2-weighted and susceptibility-weighted (SW) MR images 2, 24, 48, and 96 h after striatal whole-blood injection (representative example from $n = 10$). **C** Lesion site over time on H&E-stained coronal cryosections

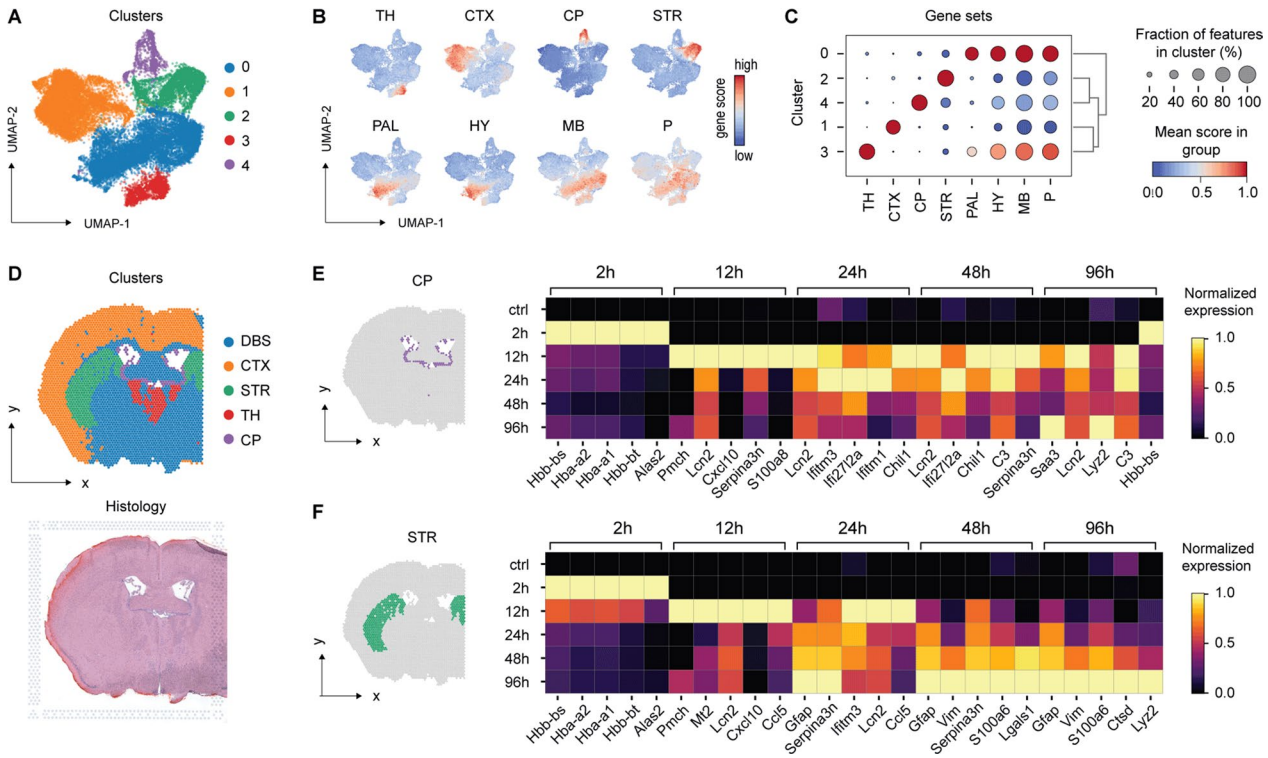


**Fig. 2** Spatiotemporal differential gene expression after striatal whole-blood injection. **A** UMAP plot colored by the unsupervised clustering of the merged spatial transcriptome dataset, including all features from $n = 6$ mice (no striatal injection [control], different time points after striatal whole-blood injection [2, 12, 24, 48, 96 h]). **B** Gene set scores for specific anatomical compartments projected on the UMAP plot. *TH* thalamus, *CTX* cortex, *CP* choroid plexus, *STR* striatum, *PAL* pallidum, *HY* hypothalamus, *MB* midbrain, *P* Pons. **C** Mean anatomical gene set expression score (*dot color*) and fraction of positive features (*dot size*) of each identified cluster. **D** Spatial projection of the identified clusters on the control sample (top) and corresponding H&E histology (bottom). **E** Top five differentially expressed genes (control as baseline) in the CP cluster stratified by time point after injection. **F** Top five differentially expressed genes (control as baseline) in the STR stratified by time point after injection

the CP epithelium but not the brain parenchyma [18], and the prototypical leukocyte adhesion molecule, Icam1, demonstrated a peak in the CP 12 h after striatal whole-blood injection (Fig. 3E, F). The pan-leukocyte marker Ptprc (Cd45) showed a biphasic CP expression with an initial increase at 24 h followed by a second peak at 96 h (Fig. 3G). Spatial gene expression revealed an acute inflammatory CP activation characterized by upregulation of interferon response elements, CCL20, adhesion molecules, and leukocyte markers. This acute CP response precedes the macrophage-dominated inflammation in the perilesional area.

### Inflammatory CP activation precedes secondary perilesional blood–brain barrier disruption and leukocyte infiltration

Next, we quantified BBB function, leukocyte infiltration, and markers of parenchymal inflammation through the generation of average-intensity maps 2, 12, 24, 48, and 96 h after striatal whole-blood injection, representing a quantitative summary of fluorophore accumulation and distribution (Fig. 4A). The permeability of the BBB was measured by the perilesional extravasation of dextran (10, 70, and 155 kDa). Both the extravasation area size (Fig. 4B, C) and fluorescence

(See figure on next page.)

**Fig. 3** Perilesional and CP transcription profiles after striatal whole-blood injection. **A** Violin plots of the temporally resolved log2-normalized expression of selected genes in the CP (violet) and the striatum (STR) (green) ($n = 6$). **B**–**D** Spatial projection of the log2-normalized expression of Ifi27l2a (**B**), Vcam1 (**C**), and Lyz2 (**D**) in the control sample and at different time points after whole-blood injection. E–G. Temporal dynamics of the log2-normalized expression of Icam1 (**E**), Ccl20 (**F**) and Ptprc (CD45) (**G**) in the CP visualized as violin plots and spatial gene expression plot

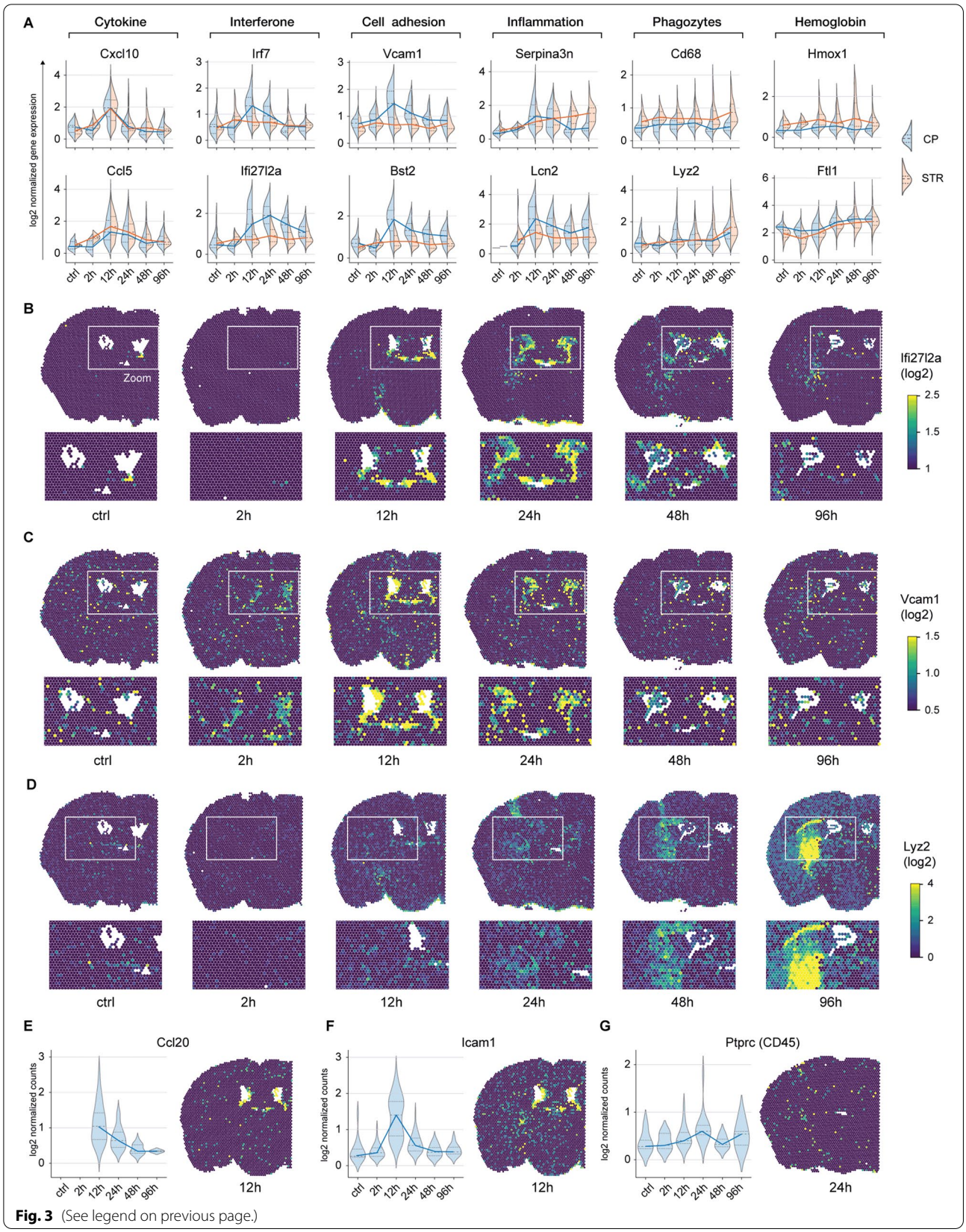


**Fig. 3** (See legend on previous page.)

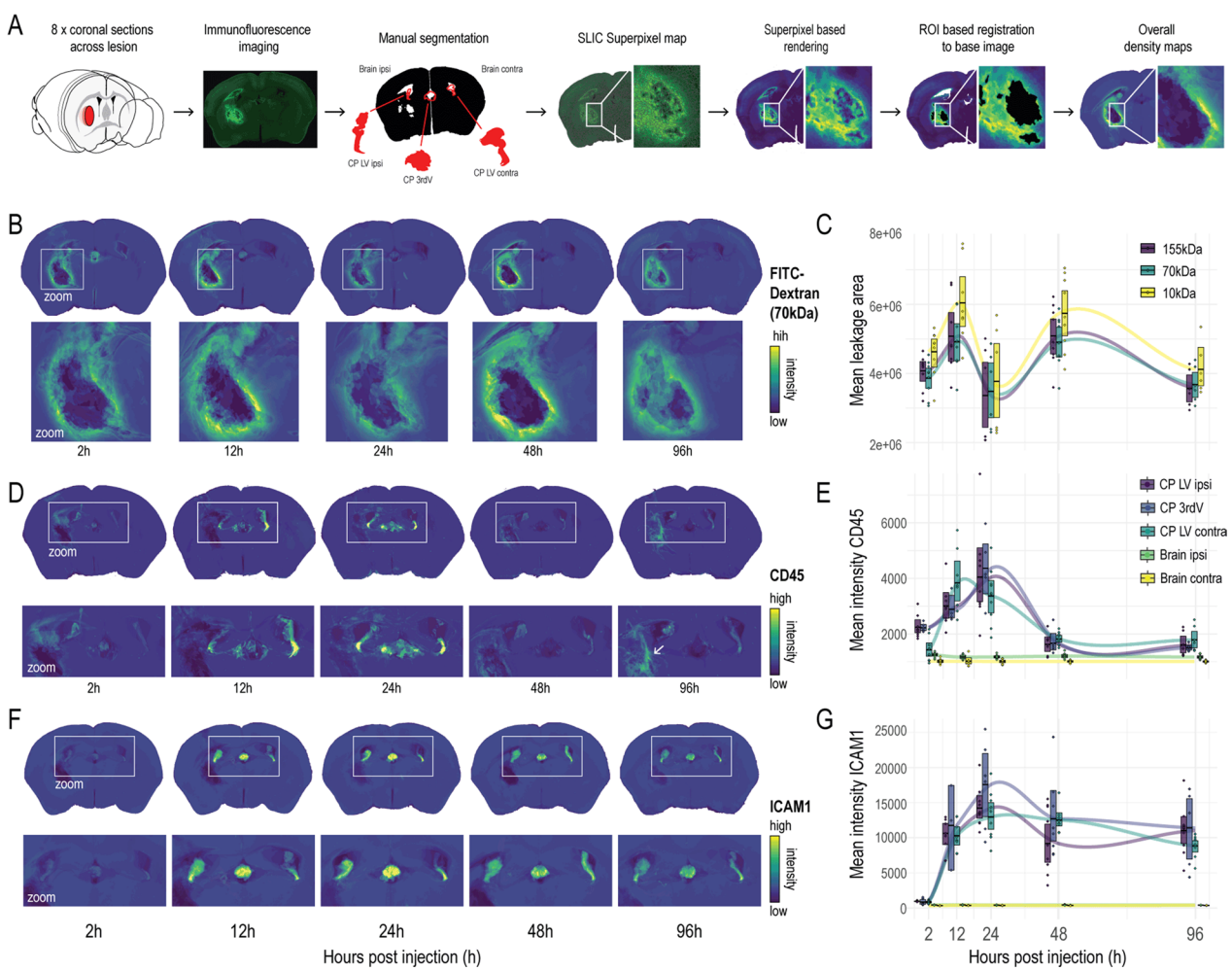


**Fig. 4** Dextran extravasation and inflammatory protein expression after striatal whole-blood injection. **A** Methodological steps of the semi-automated quantification of spatial protein expression ($n = 21$). **B** FITC-Dextran (70 kDa) average-intensity-maps at different time points with perilesional zoom-in. **C** Temporal dynamics of the mean leakage area for different dextrans (155 kDa, 70 kDa, 10 kDa). **D** CD45 average-intensity-maps at different time points with a CP/perilesional zoom-in. The arrow at 96 h indicates the high perilesional CD45 signal intensity. **E** Temporal dynamics of the mean CD45 signal intensity in different anatomical compartments. *LV* lateral ventricle, *3rdV* third ventricle. **F** ICAM1 average-intensity-maps at different time points with CP zoom-in. **G** Temporal dynamics of the mean ICAM1 signal intensity in different anatomical compartments

intensity (Fig. 4B, Additional file 1: Fig. S2A) showed a biphasic temporal course. The extravasation area size had a first peak after 12 h and a second peak after 48 h. Also extravasation fluorescence intensity showed an early peak (2–12 h) and a delayed peak 48 h after injection. The fluorescent signal of dextran in the CP differed between anatomical locations with the highest values in the ipsilateral CP ($CP_{ipsi} > CP_{third} > CP_{contra}$) at the 2 h time point (Additional file 1: Fig. S2B–D). The biphasic temporal profile of dextran extravasation is best explained by an acute mechanical disruption of the perilesional BBB causing the first leakage peak, followed by an inflammation-driven secondary spike around 48 h after injection.

Leukocyte infiltration and parenchymal inflammation were visualized by immunofluorescence for the pan-leukocyte antigen CD45 and the adhesion molecule ICAM1. Compared to all other brain regions, there was a uniquely intense CD45 signal in the CP peaking at 24 h (Fig. 4D, E). In contrast, the CD45 signal at the site of the hematoma displayed a delayed appearance starting at 48 h and markedly increasing at 96 h after injection (Fig. 4D, arrow), coinciding with the secondary lesion phenotype changes seen on MRI and in RNA expression. Similarly,

ICAM1 displayed an intense and acute expression in the CP but not in the other brain regions. A strong ICAM1 signal was already clearly detectable after 12 h and reached its peak at 36 h post-injection (Fig. 4F, G, Additional file 1: Fig. S2E shows co-staining for collagen IV as internal control).

Representative topographic antigen representation by confocal microscopy is given in Fig. 5. Dextran showed a diffuse distribution in the CP stroma and accumulation in Iba1-positive cells 2 h after intracerebral injection of whole blood and intraperitoneal administration of dextran. We found scarce CD45-positive cells within the CP 2 h post-injection, while CD45-positive cells were abundant in the CP stroma at 24 h (Fig. 5A). These cells were positive for F4/80 but negative for Iba1 and TMEM119, consistent with a phenotype of blood monocyte-derived macrophages (Fig. 5B). Correspondingly, ICAM1 expression was low in the CP 2 h after whole-blood injection, followed by a striking increase after 24 h. ICAM1 was primarily expressed on the CSF surface of the CP epithelium (Fig. 5C). At 24 h post-injection, abundant Iba1-positive cells appeared at the CSF surface of the CP epithelium (Fig. 5D). Since no F4/80-positive, or TMEM119-positive cells were detected at the CSF surface of the CP epithelium (Fig. 5B), they most likely represent Kolmer's epiplexus cells. Coincident with the macrophage infiltration signal in the spRNAseq data and the delayed signal

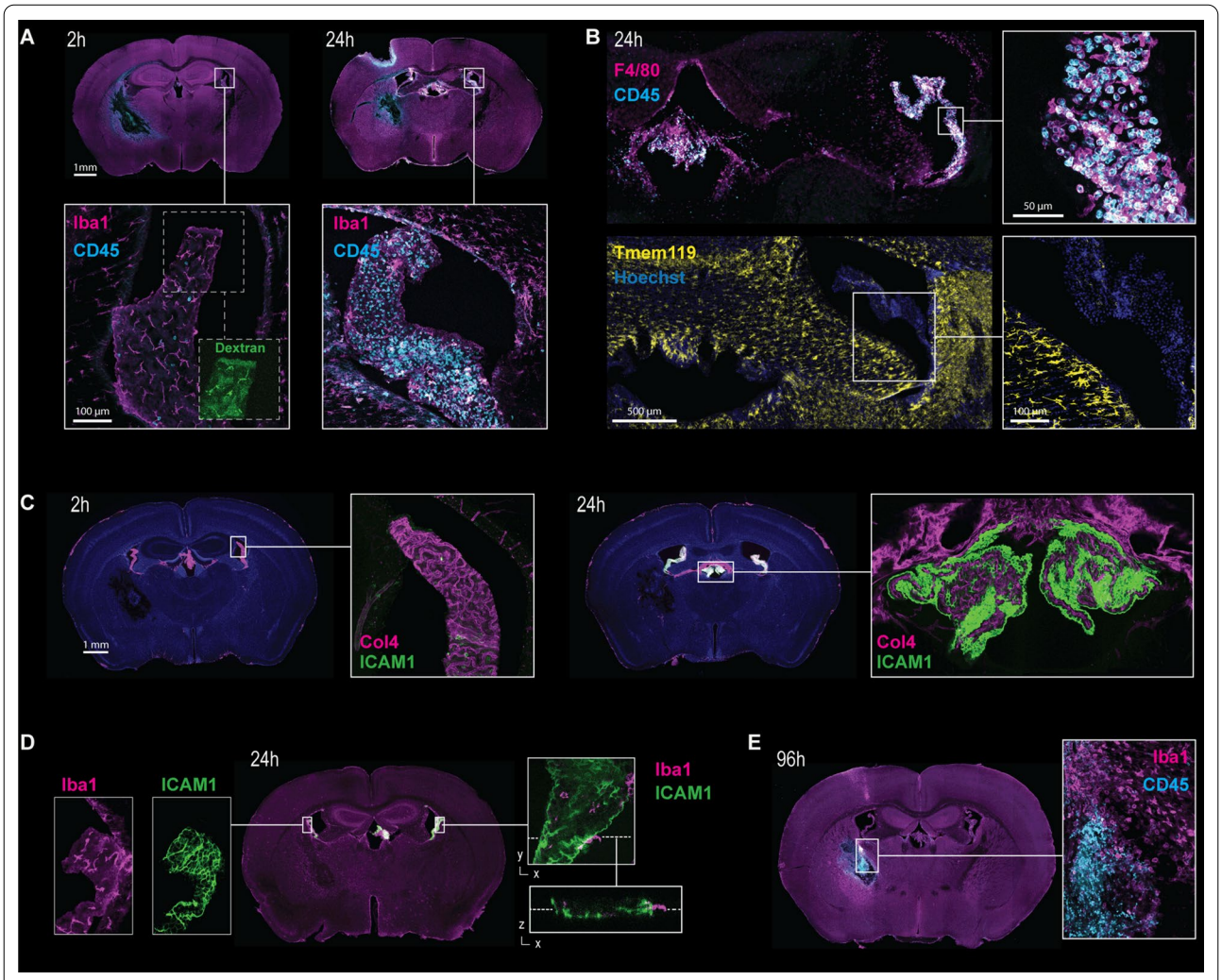


**Fig. 5** Representative immunohistology after striatal whole-blood injection. Representative vibratome sections at various time points after whole-blood injection. **A** 2 h (left) and 24 h (right) stained for Iba1 (magenta), CD45 (cyan) and dextran (green). **B** 24 h stained for F4/80 (magenta) and CD45 (cyan) or TMEM119 (yellow) and nuclei (blue). **C** 2 h (left) and 24 h (right) stained for collagen IV (Col4, magenta) and ICAM1 (cyan). **D** 24 h stained for Iba1 (magenta) and ICAM1 (green). **E** 96 h stained for Iba1 (magenta) and CD45 (cyan)

alteration in MRI, we observed a perilesional increase of CD45-positive cells at 96 h (Fig. 5E).

Collectively, immunohistological analyses showed that striatal whole-blood injection triggered an acute inflammatory response of the CP with pronounced epithelial ICAM1 expression, epiplexus macrophage lining, and stromal leukocyte invasion. This acute CP response was followed by delayed secondary perilesional dextran extravasation and leukocyte infiltration.

#### MyD88-TLR4 gene deletion attenuates acute inflammatory CP activation after striatal whole-blood injection

Finally, we defined the signaling pathway linking striatal whole-blood injection and the inflammatory activation of the CP. Enrichment analysis of the spatial gene expression data set, using selected *KEGG 2019 mouse* [19] gene sets, identified significant enrichment of the toll-like receptor signaling pathway (Fig. 6A). More specifically, we found a distinct temporal association of the acute inflammatory CP response with the post-injection dynamics of the scored expression of a MyD88-dependent TLR signaling gene set (GO:0002755) [20] (Fig. 6B, C). This analysis was consistent with the outcome of experiments in TLR4 and MyD88 knockout mice (Fig. 6D–G). Compared to wild-type littermates, ICAM1 expression and infiltration of F4/80-positive leukocytes at 24 h post whole-blood injection were markedly reduced in the CP of both mouse models, almost to the level observed in sham animals injected with saline. The same effect with lower ICAM1 expression and F4/80-positive leukocytes at 24 h post whole-blood injection was observed in the brain parenchyma (inserts Fig. 6D–G).

## Discussion

This study explored the spatial and temporal dynamics of inflammatory processes after ICH in a striatal whole-blood injection mouse model using 7-Tesla MRI, spRNAseq, functional BBB assessment, and immunofluorescence average-intensity-mapping.

Consistent with the delayed onset of perihemorrhagic edema in ICH patients, we observed a delayed secondary perilesional inflammation and BBB dysfunction in our model. On MRI, this was evidenced by changes in the T2-weighted signal intensity at the injection site after 48–96 h. This imaging pattern correlated with a delayed increase in perilesional dextran extravasation, upregulation of proinflammatory cytokine genes (e.g., CXCL10, CCL5), recurrent astrocyte activation, and pronounced macrophage infiltration. Our results on the delayed perilesional response are consistent with previous reports on secondary inflammatory processes after ICH [21, 22].

Secondary perilesional inflammation was preceded by a distinct inflammatory activation of the CP peaking at 12–24 h post-injection. We identified a remarkable upregulation of leukocyte adhesion molecules on the apical surface of the CP and an increase in the number of Kolmer's epiplexus cells within hours after striatal whole-blood injection. Simultaneously, there was a marked stromal accumulation of F4/80-positive and TMEM119-negative leukocytes, presumably reflecting the peripheral blood recruitment of monocyte-derived macrophages, which play a key role in early hematoma resolution and detoxification of its degradation products [23].

The CP occupies a strategic anatomical location covering an enormous contact area with both the CSF and peripheral circulation, combined with an extensive perfusion. Therefore, the CP might fulfill a pivotal function in CNS immune surveillance by serving as an immunological interface orchestrating and regulating inflammatory processes in the brain. High amounts of MHC class II expressing myeloid cells have been described on either side of the BCSFB with bone-marrow derived macrophages and dendritic cell in the CP stroma [24–26], and Kolmer's epiplexus cells on the apical surface of the CP epithelium [26–28].

Kolmer's epiplexus cells are believed to act as CSF antigen scavengers, thereby ensuring immunosurveillance of virtually the entire CNS [29]. Cell adhesion molecules were previously shown to be constitutively expressed on the apical CP epithelium and upregulated in experimental autoimmune encephalomyelitis [30], experimental ischemic insult [31], and even in remote CNS pathology, such as spinal cord injury [32]. Since even in healthy individuals there are 150,000–750,000 immune cells present in the CSF [33], this apical upregulation of leukocyte adhesion molecules may serve to intercept free-floating immune cells within the CSF-compartment and thus integrating information on the presence of antigens, disease associated patterns and signaling molecules from the entire CNS in the CP. We showed that the CP-specific expression of leukocyte adhesion molecules (Icam1, Vcam1) was paralleled by a specific expression of CCL20. CCL20 is the only known ligand for the chemokine receptor CCR6, and has previously been shown to be constitutively expressed by CP epithelial cells, but not by endothelial cells [18]. CCR6 activation induces a strong chemotactic response [34–36]. Collectively, the activated CP may serve as a central immunological organ of the brain through the expression of specific chemokines (e.g., CCL20) and the epithelial upregulation of leukocyte adhesion molecules (e.g., ICAM1, VCAM1) to mobilize and scavenge inflammatory cells from the CSF.

CP epithelial cells reportedly possess the capacity to produce chemokines for systemic immune cell attraction upon both central and peripheral noxious stimuli [9, 37]. Our spRNAseq data showed an early and

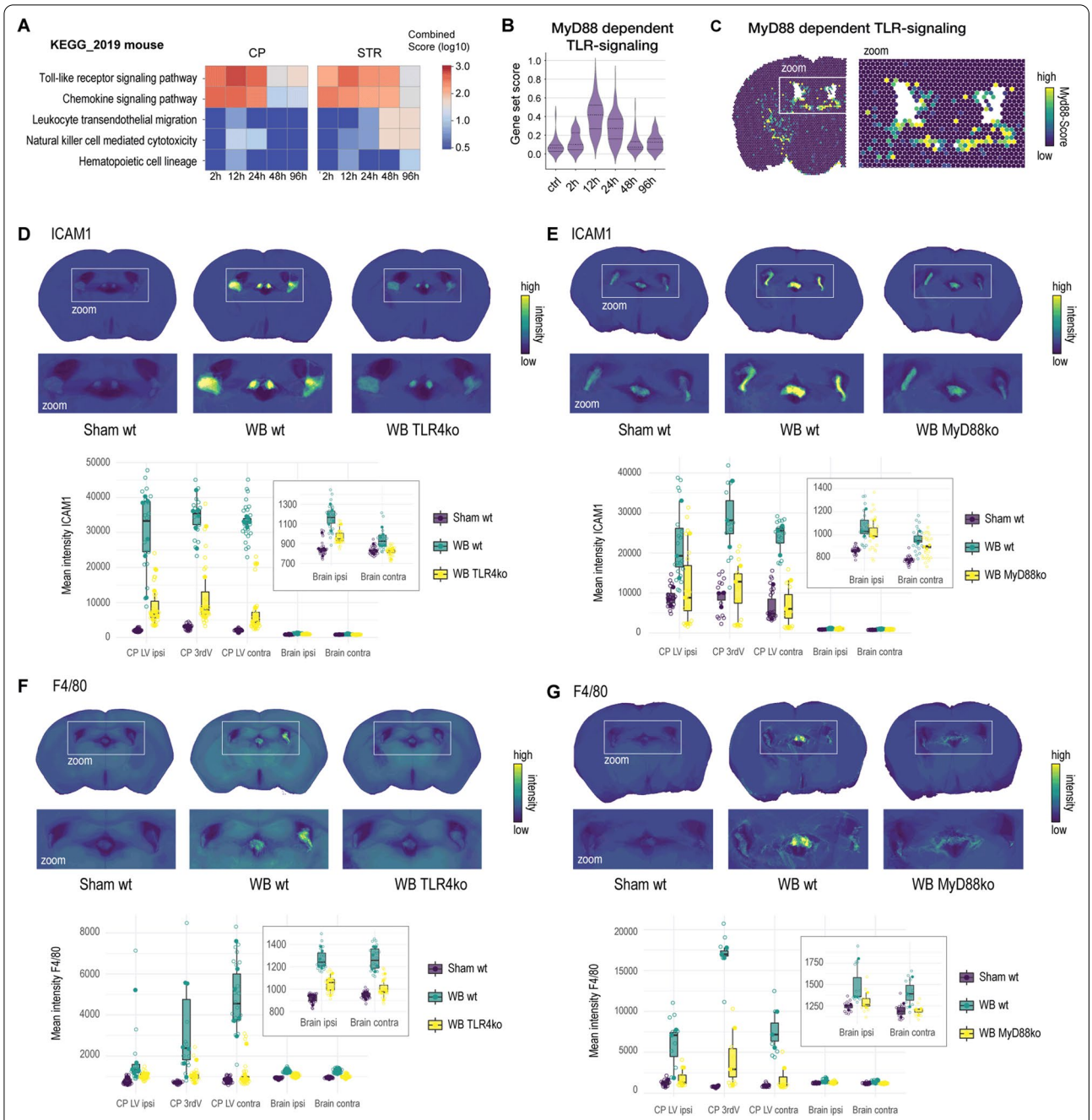


**Fig. 6** MyD88-TLR4 dependence of the CP response after striatal whole-blood injection. **A** *KEGG-2019* mouse-based gene-set enrichment patterns in the CP and the striatum (STR) (control as baseline, $n=6$). **B** Temporal dynamics of the *MyD88-dependent-TLR4-signaling* gene set score in the CP ($n=6$). **C** Spatial projection of the *MyD88-dependent-TLR4-signaling* gene set score 24 h after injection. **D** ICAM1 signal intensity 24 h after striatal NaCl (sham, $n=6$) or whole-blood ($n=6$) injection in littermate TLR4+/+ mice (wt), and whole-blood injection in TLR4−/− (TLR4ko) mice ($n=6$). Top: ICAM1 density-maps with a CP zoom-in. Bottom: Mean ICAM1 signal intensity in different anatomical compartments. *LV, lateral ventricle; 3rdV, third ventricle.* **E** ICAM1 signal intensity 24 h after striatal NaCl (sham) or whole-blood injection in littermate MyD88+/+ mice (wild-type), and whole-blood injection in MyD88 knockout (MyD88ko) mice ($n=8$ per group). Top: ICAM1 density-maps with a CP zoom-in. Bottom: Mean ICAM1 signal intensity in different anatomical compartments. **F** F4/80 signal intensity 24 h after striatal NaCl (sham) or whole-blood injection in littermate TLR4+/+ mice (wild-type), and whole-blood injection in TLR4 knockout (TLR4ko) mice ($n=6$ per group). Top: F4/80 density-maps with a CP zoom-in. Bottom: Mean F4/80 signal intensity in different anatomical compartments. **G** F4/80 signal intensity 24 h after striatal NaCl (sham or whole-blood injection in littermate MyD88+/+ mice (wt), and whole-blood injection in MyD88−/− (MyD88ko) mice ($n=8$ per group). Top: F4/80 density-maps with a CP zoom-in. Bottom: Mean F4/80 signal intensity in different anatomical compartments

high CP expression of chemoattractants, most dominantly CXCL10 and CCL5. CXCL10 and CCL5 attract blood monocytes and lymphocytes, and promotes their endothelial adhesion [38–40]. The CP, the most perfused structure of the brain [12], might therefore serve as an interface between peripheral leukocytes and CNS antigen presenting cells, possibly promoting secondary infiltration at the lesion site. Whether the CP serves only as an immunological interface or even as a gateway for immune cells into the CNS, as hypothesized for example after traumatic brain injury, remains to be clarified [9, 37].

We established that the pronounced inflammatory activation of the CP after striatal whole-blood injection is dependent on MyD88-TLR4 signaling. There is a high level of TLR4 expression on the CP epithelium [41]. In addition, CSF hypersecretion after intraventricular whole-blood injection depends on TLR4 signaling in the CP epithelium [42]. Our spRNAseq data demonstrated a distinct temporal association between MyD88-dependent TLR signaling in the CP and its expression of adhesion molecules and chemoattractants. In MyD88 and TLR4 knockout mice, there was neither CP surface activation nor stromal leukocyte invasion after striatal whole-blood injection. In line with our findings, ICAM1, CCL20, CXCL10, and CCL5 expressions reportedly depend on MyD88-TLR4 signaling in other organs [43–46]. The CP thus appears to respond in a TLR4-dependent manner to intracranial hemorrhage with epithelial upregulation of adhesion molecules, release of centrally and peripherally oriented chemoattractants, and CSF hypersecretion.

Future studies are needed to define the nature of the specific TLR4 ligands and the precise site of their action. Currently, we can speculate that the tissue damage caused by the acute bleeding releases multiple tissue damage-associated molecular patterns (DAMPs) into the interstitial space of the brain. Additionally, the lysis of erythrocytes may liberate large quantities of cell-free hemoglobin into the brain, which is prone to oxidation and release of free radicals and the TLR4 agonist heme [15, 47–52]. Mature erythrocytes still contain detectable hemoglobin transcripts, which can be used in transcriptome-based studies as a marker for the distribution of red blood cell components [53]. We detected high levels of hemoglobin subunit transcripts in the CP as early as 2 h after the striatal injection of whole-blood. If taken as a surrogate marker for all locally released DAMPs, this observation suggests a rapid transfer of signaling molecules from the lesion site to the CP epithelium, which acts in this mechanistic model as a sensor for remote brain injury, triggering downstream inflammation, CSF hypersecretion, and leukocyte infiltration from the peripheral circulation.

There are certain limitations to be considered while interpreting the results of our study. We based our data solely on a whole-blood injection model for ICH. Injection of bacterial collagenase is another established ICH model in rodents [54]. We adopted the whole-blood injection model because it allowed a more isolated investigation of brain exposure to blood, the relative hematoma volume could be easily adjusted to the human clinical correlate, and the lesion size demonstrated high reproducibility. In addition, although the blood was injected under stereotactic guidance into the right striatum, 30% of the initial SWI showed evidence for an intraventricular hemorrhage. This results in some variability of the model and might influence the inflammatory CP response. Our model is, however, in line with the clinical situation in humans, where 19–55% of patients with ICH have intraventricular blood [55]. Furthermore, we deliberately refrained from quantifying the MRI data and instead presented them only qualitatively, as no 3D datasets were collected. The interpretability of the dextran signal in the CP in our study is limited. The dextran was applied intraperitoneally 2 h before euthanasia. The CP signal likely represents the sum of extravasated dextran derived from CP stroma capillaries due to blood–CSF barrier disruption and CSF-derived dextran from the lesion site. Finally, due to the size restrictions of the active surface of the Visium slide, it was not possible to obtain the spRNAseq data from a full coronal brain section and therefore the contralateral hemisphere is only partially represented in the data.

Collectively, this study enhances our understanding of the spatial and temporal dynamics of inflammatory processes after ICH. The pronounced and early reaction of the CP, preceding secondary perilesional inflammation and edema, positions the MyD88-TLR4-dependent immunological CP activation as a potential target to modulate ICH-SBI.

#### Abbreviations

BBB: Blood–brain barrier; CP: Choroid plexus; ICH-SBI: Intracerebral hemorrhage related secondary brain injury; MRI: Magnetic resonance imaging; MyD88: Myeloid differentiation factor 88; PBS: Phosphate buffered saline; ROI: Region of interest; spRNAseq: Spatial RNA sequencing; TLR4: Toll-like receptor 4.

## Supplementary Information

The online version contains supplementary material available at https://doi.org/10.1186/s12974-022-02641-5.

**Additional file 1.** Additional methods. **Table S1.** Details of the different fluorescently labeled dextrans used to assess the blood–brain barrier function. **Table S2.** The specific antibodies used for immunostaining and their dilutions. **Fig S1.** Spatial projection of unsupervised clusters. **Fig S2.** Temporal course of perilesional dextran extravasation, leukocytosis and ICAM1 signal intensity.

**Acknowledgements**
We thank the staff of the Functional Genomic Center Zurich for their support with transcriptome analysis, Marc-Aurel Augath of the Institute for Biomedical Engineering (University of Zurich and ETH Zurich) for his technical assistance during the MRI studies.

**Author contributions**
Conceptualization: KA, RMB, MH, DJS; methodology: KA, RMB, JK; investigation: KA, RMB, BRT, NiS, NaS, LB, KH; formal analysis: KA, RMB, BRT; visualization and writing original draft: KA, RMB, writing—review and editing: all authors; funding acquisition: KA, RMB, FV, MH, DJS; resources: JK, MH, DJS. All authors read and approved the final manuscript.

**Funding**
This study was supported by the Swiss National Science Foundation (4221-06-2017 to RMB, 310030_201202/1 to FV, 310030_197823 to DJS and MH), Innosuisse (36361 IP-LS), the Uniscientia Foundation, the Candoc of the University of Zurich (20-025 to RMB and 21-021 to KA), and CSL Behring.

**Availability of data and materials**
The Fiji-script, processed spRNAseq-data, python script, and R-code to reproduce all analyses and plots are available online (https://doi.org/10.5281/zenodo.5760872).

## Declarations

**Ethics approval and consent to participate**
All experiments were approved by the Swiss Federal Veterinary Office (ZH89/2019).

**Consent for publication**
Not applicable.

**Competing interests**
The authors report no competing interests.

**Author details**
[1]Department of Neurosurgery, Clinical Neuroscience Center, Universitätsspital and University of Zurich, Frauenklinikstrasse 10, 8091 Zurich, Switzerland. [2]Division of Internal Medicine, Universitätsspital and University of Zurich, Zurich, Switzerland. [3]Institute for Biomedical Engineering, University of Zurich and ETH Zurich, Zurich, Switzerland.

Received: 21 September 2022 Accepted: 10 November 2022
Published online: 08 December 2022

**References**

1. Feigin VL, Krishnamurthi RV, Parmar P, Norrving B, Mensah GA, Bennett DA, et al. Update on the global burden of ischemic and hemorrhagic stroke in 1990–2013: the GBD 2013 study. Neuroepidemiology. 2015;45:161–76.
2. Andersen KK, Olsen TS, Dehlendorff C, Kammersgaard LP. Hemorrhagic and ischemic strokes compared: stroke severity, mortality, and risk factors. Stroke. 2009;40:2068–72.
3. Xi G, Keep RF, Hoff JT. Mechanisms of brain injury after intracerebral haemorrhage. Lancet Neurol. 2006;5:53–63.
4. Volbers B, Giede-Jeppe A, Gerner ST, Sembill JA, Kuramatsu JB, Lang S, et al. Peak perihemorrhagic edema correlates with functional outcome in intracerebral hemorrhage. Neurology. 2018;90:e1005–12.
5. Keep RF, Hua Y, Xi G. Intracerebral haemorrhage: mechanisms of injury and therapeutic targets. Lancet Neurol. 2012;11:720–31.
6. Hemorrhagic Stroke Academia Industry (HEADS) Roundtable Participants, Second HEADS Roundtable Participants. Recommendations for clinical trials in ICH: the second hemorrhagic stroke academia industry roundtable. Stroke. 2020;51:1333–8.
7. Engelhardt B, Vajkoczy P, Weller RO. The movers and shapers in immune privilege of the CNS. Nat Immunol. 2017;18:123–31.
8. Solár P, Zamani A, Kubíčková L, Dubový P, Joukal M. Choroid plexus and the blood–cerebrospinal fluid barrier in disease. Fluids Barriers CNS. 2020;17:35.
9. Szmydynger-Chodobska J, Strazielle N, Zink BJ, Ghersi-Egea J-F, Chodobski A. The role of the choroid plexus in neutrophil invasion after traumatic brain injury. J Cereb Blood Flow Metab. 2009;29:1503–16.
10. Ghersi-Egea J-F, Strazielle N, Catala M, Silva-Vargas V, Doetsch F, Engelhardt B. Molecular anatomy and functions of the choroidal blood-cerebrospinal fluid barrier in health and disease. Acta Neuropathol. 2018;135:337–61.
11. Keep RF, Jones HC. A morphometric study on the development of the lateral ventricle choroid plexus, choroid plexus capillaries and ventricular ependyma in the rat. Brain Res Dev Brain Res. 1990;56:47–53.
12. Szmydynger-Chodobska J, Chodobski A, Johanson CE. Postnatal developmental changes in blood flow to choroid plexuses and cerebral cortex of the rat. Am J Physiol. 1994;266:R1488–92.
13. R Core Team. R: A language and environment for statistical computing. Vienna, Austria: R Foundation for Statistical Computing; 2020. https://www.R-project.org/. Accessed 4 Aug 2020.
14. Akeret K, Hugelshofer M, Schaer DJ, Buzzi RM. Spatial transcriptome data from coronal mouse brain sections after striatal injection of heme and heme-hemopexin. Data Brief. 2022. https://doi.org/10.1016/j.dib.2022.107866.
15. Buzzi RM, Akeret K, Schwendinger N, Klohs J, Vallelian F, Hugelshofer M, et al. Spatial transcriptome analysis defines heme as a hemopexin-targetable inflammatoxin in the brain. Free Radic Biol Med. 2022;1(179):277–87.
16. Fang Z, Wolf A, Liao Y, McKay A, Fröhlich F, Reese F; Kimmel J, engelsdaniel, Xiaohui L, pirakd, sorrge. zqfang/GSEApy: gseapy-v0.10.7 (v0.10.7). Zenodo; 2021. https://doi.org/10.5281/zenodo.5708913.
17. Lein ES, Hawrylycz MJ, Ao N, Ayres M, Bensinger A, Bernard A, et al. Genome-wide atlas of gene expression in the adult mouse brain. Nature. 2007;445:168–76.
18. Reboldi A, Coisne C, Baumjohann D, Benvenuto F, Bottinelli D, Lira S, et al. C-C chemokine receptor 6-regulated entry of TH-17 cells into the CNS through the choroid plexus is required for the initiation of EAE. Nat Immunol. 2009;10:514–23.
19. Kanehisa M, Furumichi M, Sato Y, Ishiguro-Watanabe M, Tanabe M. KEGG: integrating viruses and cellular organisms. Nucleic Acids Res. 2021;49:D545–51.
20. Gene Ontology Consortium. The gene ontology resource: enriching a GOld mine. Nucleic Acids Res. 2021;49:D325–34.
21. Yao Y, Tsirka SE. Chemokines and their receptors in intracerebral hemorrhage. Transl Stroke Res. 2012;3:70–9.
22. Zhu H, Wang Z, Yu J, Yang X, He F, Liu Z, et al. Role and mechanisms of cytokines in the secondary brain injury after intracerebral hemorrhage. Prog Neurobiol. 2019;178: 101610.
23. Humar R, Schaer DJ, Vallelian F. Erythrophagocytes in hemolytic anemia, wound healing, and cancer. Trends Mol Med. 2022;S1471–4914(22):00210–6.
24. Serot JM, Foliguet B, Béné MC, Faure GC. Ultrastructural and immunohistological evidence for dendritic-like cells within human choroid plexus epithelium. NeuroReport. 1997;8:1995–8.
25. Nathanson JA, Chun LL. Immunological function of the blood-cerebrospinal fluid barrier. Proc Natl Acad Sci U S A. 1989;86:1684–8.
26. Nataf S, Strazielle N, Hatterer E, Mouchiroud G, Belin M-F, Ghersi-Egea J-F. Rat choroid plexuses contain myeloid progenitors capable of differentiation toward macrophage or dendritic cell phenotypes. Glia. 2006;54:160–71.
27. Ling EA, Kaur C, Lu J. Origin, nature, and some functional considerations of intraventricular macrophages, with special reference to the epiplexus cells. Microsc Res Tech. 1998;41:43–56.
28. Goldmann T, Wieghofer P, Jordão MJC, Prutek F, Hagemeyer N, Frenzel K, et al. Origin, fate and dynamics of macrophages at central nervous system interfaces. Nat Immunol. 2016;17:797–805.
29. Engelhardt B, Ransohoff RM. Capture, crawl, cross: the T cell code to breach the blood–brain barriers. Trends Immunol Elsevier. 2012;33:579–89.
30. Steffen BJ, Breier G, Butcher EC, Schulz M, Engelhardt B. ICAM-1, VCAM-1, and MAdCAM-1 are expressed on choroid plexus epithelium but not

endothelium and mediate binding of lymphocytes in vitro. Am J Pathol. 1996;148:1819–38.
31. Ge R, Tornero D, Hirota M, Monni E, Laterza C, Lindvall O, et al. Choroid plexus-cerebrospinal fluid route for monocyte-derived macrophages after stroke. J Neuroinflammation. 2017;14:153.
32. Shechter R, Miller O, Yovel G, Rosenzweig N, London A, Ruckh J, et al. Recruitment of beneficial M2 macrophages to injured spinal cord is orchestrated by remote brain choroid plexus. Immunity. 2013;38:555–69.
33. Kivisäkk P, Mahad DJ, Callahan MK, Trebst C, Tucky B, Wei T, et al. Human cerebrospinal fluid central memory CD4+ T cells: evidence for trafficking through choroid plexus and meninges via P-selectin. Proc Natl Acad Sci U S A. 2003;100:8389–94.
34. Nelson RT, Boyd J, Gladue RP, Paradis T, Thomas R, Cunningham AC, et al. Genomic organization of the CC chemokine mip-3alpha/CCL20/larc/exodus/SCYA20, showing gene structure, splice variants, and chromosome localization. Genomics. 2001;73:28–37.
35. Schutyser E, Struyf S, Menten P, Lenaerts JP, Conings R, Put W, et al. Regulated production and molecular diversity of human liver and activation-regulated chemokine/macrophage inflammatory protein-3 alpha from normal and transformed cells. J Immunol. 2000;165:4470–7.
36. Röhrl J, Yang D, Oppenheim JJ, Hehlgans T. Specific binding and chemotactic activity of mBD4 and its functional orthologue hBD2 to CCR6-expressing cells. J Biol Chem. 2010;285:7028–34.
37. Szmydynger-Chodobska J, Gandy JR, Varone A, Shan R, Chodobski A. Synergistic interactions between cytokines and AVP at the blood-CSF barrier result in increased chemokine production and augmented influx of leukocytes after brain injury. PLoS ONE. 2013;8: e79328.
38. Luster AD, Unkeless JC, Ravetch JV. Gamma-interferon transcriptionally regulates an early-response gene containing homology to platelet proteins. Nature. 1985;315:672–6.
39. Dufour JH, Dziejman M, Liu MT, Leung JH, Lane TE, Luster AD. IFN-gamma-inducible protein 10 (IP-10; CXCL10)-deficient mice reveal a role for IP-10 in effector T cell generation and trafficking. J Immunol. 2002;168:3195–204.
40. Appay V, Rowland-Jones SL. RANTES: a versatile and controversial chemokine. Trends Immunol. 2001;22:83–7.
41. Chakravarty S, Herkenham M. Toll-like receptor 4 on nonhematopoietic cells sustains CNS inflammation during endotoxemia, independent of systemic cytokines. J Neurosci. 2005;25:1788–96.
42. Gram M, Sveinsdottir S, Cinthio M, Sveinsdottir K, Hansson SR, Mörgelin M, et al. Extracellular hemoglobin - mediator of inflammation and cell death in the choroid plexus following preterm intraventricular hemorrhage. J Neuroinflammation. 2014;11:200.
43. Klein M, Brouwer MC, Angele B, Geldhoff M, Marquez G, Varona R, et al. Leukocyte attraction by CCL20 and its receptor CCR6 in humans and mice with pneumococcal meningitis. PLoS ONE. 2014;9: e93057.
44. Lu Z, Li Y, Jin J, Zhang X, Lopes-Virella MF, Huang Y. Toll-like receptor 4 activation in microvascular endothelial cells triggers a robust inflammatory response and cross talk with mononuclear cells via interleukin-6. Arterioscler Thromb Vasc Biol. 2012;32:1696–706.
45. Kang S, Lee S-P, Kim KE, Kim H-Z, Mémet S, Koh GY. Toll-like receptor 4 in lymphatic endothelial cells contributes to LPS-induced lymphangiogenesis by chemotactic recruitment of macrophages. Blood. 2009;113:2605–13.
46. Song Y, Fullerton DA, Mauchley D, Su X, Ao L, Yang X, et al. Microfilaments facilitate TLR4-mediated ICAM-1 expression in human aortic valve interstitial cells. J Surg Res. 2011;166:52–8.
47. Akeret K, Buzzi RM, Schaer CA, Thomson BR, Vallelian F, Wang S, et al. Cerebrospinal fluid hemoglobin drives subarachnoid hemorrhage-related secondary brain injury. J Cereb Blood Flow Metab. 2021;41(11):3000–15.
48. Vallelian F, Buehler PW, Schaer DJ. Hemolysis, free hemoglobin toxicity and scavenger protein therapeutics. Blood. 2022. https://doi.org/10.1182/blood.2022015596.
49. Kwon MS, Woo SK, Kurland DB, Yoon SH, Palmer AF, Banerjee U, et al. Methemoglobin is an endogenous toll-like receptor 4 ligand-relevance to subarachnoid hemorrhage. Int J Mol Sci. 2015;16:5028–46.
50. Bücker P, Buzzi RM, Akeret K, Mosberger L, Richter H, Sperling M, et al. A model to visualize the fate of iron after intracranial hemorrhage using isotopic tracers and elemental bioimaging. Metallomics. 2022. https://doi.org/10.1093/mtomcs/mfac057.
51. Vallelian F, Schaer CA, Deuel JW, Ingoglia G, Humar R, Buehler PW, et al. Revisiting the putative role of heme as a trigger of inflammation. Pharmacol Res Perspect. 2018;6: e00392.
52. Vallelian F, Deuel JW, Opitz L, Schaer CA, Puglia M, Lönn M, et al. Proteasome inhibition and oxidative reactions disrupt cellular homeostasis during heme stress. Cell Death Differ. 2015;22:597–611.
53. Pfefferlé M, Ingoglia G, Schaer CA, Yalamanoglu A, Buzzi R, Dubach IL, et al. Hemolysis transforms liver macrophages into antiinflammatory erythrophagocytes. J Clin Invest. 2020;130:5576–90.
54. MacLellan CL, Silasi G, Auriat AM, Colbourne F. Rodent models of intracerebral hemorrhage. Stroke. 2010;41:S95–8.
55. Hanley DF. Intraventricular hemorrhage: severity factor and treatment target in spontaneous intracerebral hemorrhage. Stroke. 2009;40:1533–8.

## Publisher's Note